ACTA IMEKO
ISSN: 2221-870X
December 2026, Volume 15, Number 4, 1 – 8

Finite element modeling of a nominal tetrachiral lattice under quasi-static compression with preliminary insights into manufacturing-induced geometric deviations

Vito Topić Brečević[1], Emina Hadzalic[2], Veronika Drechslerová[3], Petr Koudelka[3], Daniel Kytýř[4], Zvonimir Tomičević[1]

[1] *Faculty of Mechanical Engineering and Naval Architecture, University of Zagreb, Zagreb, Croatia*
[2] *Faculty of Civil Engineering, University of Rijeka, Rijeka, Croatia*
[3] *Czech Technical University in Prague, Faculty of Transportation Sciences, Prague, Czechia*
[4] *Czech Academy of Sciences, Institute of Theoretical and Applied Mechanics, Prague, Czechia*

ABSTRACT
This study presents the finite element modeling of an SLA-manufactured tetrachiral lattice subjected to quasi-static uniaxial compression. The constitutive law of the base material was calibrated using cyclic compression tests performed on bulk specimens, providing the elastic modulus, yield stress, and true-stress–plastic-strain relationship. A three-dimensional finite element model of the nominal lattice geometry was developed in Abaqus and solved using the explicit solution scheme. The numerical predictions showed good agreement with the experimental force–displacement response during the initial stage of compression. However, the numerical model progressively overestimated the load-carrying capacity as the deformation increased. Preliminary comparison of the nominal CAD geometry with X-ray computed tomography (XCT) data revealed manufacturing-induced geometric deviations, that may contribute to the discrepancies between the numerical and experimental responses. These findings highlight the need for a finite element framework that incorporates as-manufactured geometries and representative boundary conditions derived from full-field measurements obtained using Digital Volume Correlation (DVC).

Section: RESEARCH PAPER

Keywords: tetrachiral lattice; quasi-static compression; finite element model; nominal geometry; as-manufactured geometry

Citation: V. Topić Brečević, E. Hadzalic, V. Drechslerová, P. Koudelka, D. Kytýř, Z. Tomičević, Finite element modeling of a nominal tetrachiral lattice under quasi-static compression with preliminary insights into manufacturing-induced geometric deviations, Acta IMEKO, vol. 15 (2026) no. 4, pp. 1–8. DOI: 10.21014/actaimeko.v15i4.2475

Section Editor: Jakub Svatos, CVUT Prague, Czech Republic

Received: July 29, 2026; **In Final Form:** October 21, 2026; **Published:** December 2026.

Copyright: This is an open-access article distributed under the terms of the Creative Commons Attribution 4.0 International License.

Funding: This research was supported by the Czech Science Foundation (Project No. 25-18209S), the Strategy AV21 programme “AI: Artificial Intelligence for Science and Society”, and the European Union (NextGenerationEU) under the National Recovery and Resilience Plan 2021–2026 (NRRP), through the UNIZAG FSB institutional project “Generative design based on experimental and numerical modelling - GENEXPERT”, approved by the Ministry of Science, Education and Youth of the Republic of Croatia (component C3.2, source 581).

Corresponding Author: Emina Hadzalic, e-mail: emina.hadzalic@uniri.hr

1. INTRODUCTION

Additively manufactured lattice structures have attracted significant interest across various engineering fields owing to their favorable stiffness- and strength-to-weight ratios, energy-absorbing capabilities, and adaptability to application-specific requirements. The mechanical response of these architected materials depends strongly on lattice topology, nodal connectivity, and the properties of the constituent material.

Among the various lattice topologies, auxetic structures have attracted particular attention because of their negative Poisson’s ratio and the associated deformation mechanisms. A wide range of auxetic unit-cell designs has been proposed, including re-entrant honeycombs, chiral lattices, and other architected geometries [1]–[5]. In particular, chiral lattice structures deform predominantly through ligament bending, resulting in enhanced energy absorption compared to conventional re-entrant architectures, where deformation is typically governed by bending-induced buckling [6]–[9]. Owing to these characteristics, chiral lattices have found increasing use in lightweight structural applications, including energy-absorbing fillers for hollow sections and crashworthiness-critical components [10]–[12].

Understanding the mechanical response of lattice structures and optimizing their performance for specific applications requires reliable numerical modeling capable of capturing their

complex deformation behavior under different loading conditions. The increasing availability of computational resources has established the finite element method as the primary tool for investigating the mechanical behavior of lattice structures. Depending on the required balance between computational efficiency and geometric fidelity, different discretization strategies have been adopted. To reduce computational cost, many numerical studies have employed simplified beam-based representations of lattice struts [13]–[15]. Although computationally efficient, these models often fail to accurately reproduce the geometry of the strut junctions, leading to altered deformation mechanisms and reduced prediction accuracy. Consequently, three-dimensional solid discretizations have been increasingly adopted to provide a more faithful representation of the lattice geometry and to capture local deformation mechanisms with higher fidelity [16], although they are computationally more demanding and require substantially longer computation times.

The majority of these finite element models are developed using nominal CAD geometries and idealized boundary conditions, without accounting for the geometric imperfections that are inevitably introduced during the additive manufacturing process, which may influence the predicted overall response. Several strategies have been proposed to account for manufacturing-induced imperfections in finite element models of lattice structures. These include modifications of beam-element cross-sections to represent irregular strut diameters [17], stochastic descriptions of geometric variability based on measured diameter distributions or randomly distributed defects [18]–[20], and, more recently, image-based finite element models derived directly from X-ray computed tomography (XCT), enabling the incorporation of the as-manufactured geometry. Such image-based models have been employed to investigate the quasi-static compressive response of lattice structures [21], [22].

To understand the influence of manufacturing-induced imperfections, it is first necessary to establish the baseline mechanical response of the nominal lattice geometry. The present study therefore focuses on the finite element modeling of a nominal tetrachiral auxetic lattice subjected to a quasi-static uniaxial compression. The numerical model is developed using the nominal CAD geometry under ideal loading conditions, while the material model is calibrated using experimental bulk compression tests. The numerical predictions are subsequently compared with the experimental compressive response to evaluate the applicability of the idealized model. As part of the experimental work, the undeformed manufactured lattice specimen was scanned using XCT. The acquired XCT data were reconstructed to obtain the as-manufactured lattice geometry, which was subsequently superimposed on the corresponding nominal CAD geometry to provide preliminary insights into manufacturing-induced geometric imperfections.

These observations provide a basis for future studies incorporating as-manufactured geometries and experimentally representative boundary conditions derived from Digital Volume Correlation (DVC) analyses of XCT data [23]. Such studies would extend the present modeling framework towards image-based finite element analyses informed by DVC measurements [24], [25].

The remainder of this paper is structured as follows. Section 2 outlines the experimental programme, including the characterization of the bulk material and the uniaxial compression of the tetrachiral lattice. Section 3 provides a detailed description of the finite element model. Section 4 presents the numerical results, followed by a comparison with the experimental results and a discussion of the observed response. Finally, Section 5 summarizes the main conclusions and provides recommendations for future research.

2. EXPERIMENTAL PROGRAMME

2.1. Materials and specimens

The bulk and lattice specimens were fabricated from Phrozen RPG Resin (Phrozen Technology Co., Ltd., Taiwan) using a stereolithography (SLA) 3D printer with monochrome LCD display, a 405 nm ParaLED Matrix 2.0 light source, and a bottom-up architecture variety. The nominal material properties of the resin, as reported by the manufacturer, are summarized in Table 1.

All specimens were printed with a layer thickness of 50 μm, an exposure time of 4 s per layer, and an exposure time of 35 s for the bottom layers. After printing, the specimens were post-processed by ultrasonic cleaning in isopropyl alcohol for 5 min to remove the uncured resin, followed by UV post-curing for 10 min to ensure the desired properties of the material.

Two types of specimens were manufactured for the experimental investigation: solid cylindrical bulk specimens for material characterization and tetrachiral lattice specimen for experimental assessment of the finite element model. The bulk specimens had nominal dimensions of 12 mm in diameter and 12 mm in height.

The lattice specimen consisted of periodically repeated tetrachiral unit cells with sinusoidally curved struts. The unit-cell geometry was parameterized by the horizontal and vertical half-wavelengths ($L_{\mathrm{H}} = L_{\mathrm{V}} = 1.1108\,\mathrm{mm}$) and the strut waviness amplitude ($A = 0.4\,\mathrm{mm}$). The strut diameter was 0.65 mm, forming a lattice composed of five unit cells in each spatial direction with nominal dimensions of $5 \times 5 \times 5$ mm. To ensure uniform load transfer during compression tests, solid loading platforms with thicknesses of 5 mm and 6 mm were incorporated at the top and bottom of the specimen, respectively, resulting in an overall specimen height of approximately 32 mm. The tetrachiral lattice specimen is shown in Figure 1.

2.2. Bulk material compression test

The bulk specimens were subjected to uniaxial compression using an in-house developed electromechanical loading device with a maximum loading capacity of 55 kN. Cyclic compression tests were performed under displacement control at a constant loading rate of 5 μm/s, with a final crosshead displacement of 6 mm. The cyclic tests used progressively increasing displacement levels, each followed by complete unloading to zero load.

Table 1. Nominal material properties of Phrozen RPG Resin [26].

Property	Typical value
Density in $\mathrm{g/cm^3}$	1.13
Tensile strength at break in MPa	21.7 to 24.2
Tensile modulus in MPa	960 to 1152
Elongation at break in %	25.3 to 30.6

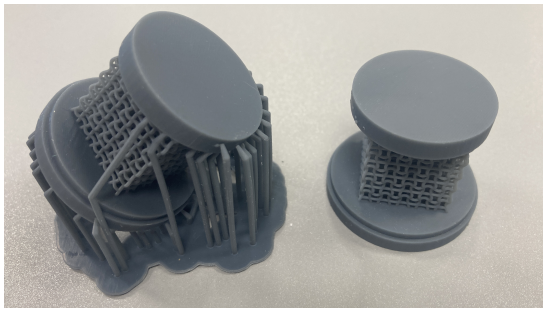


Figure 1. Tetrachiral lattice specimen fabricated using SLA 3D printing.

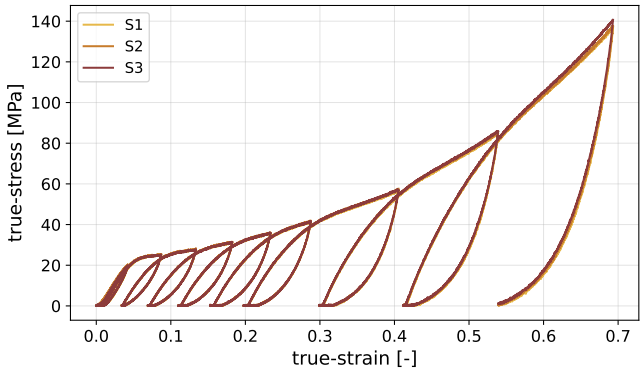


Figure 2. Experimental true-stress–true-strain curves obtained from cyclic compression tests of three bulk specimens.

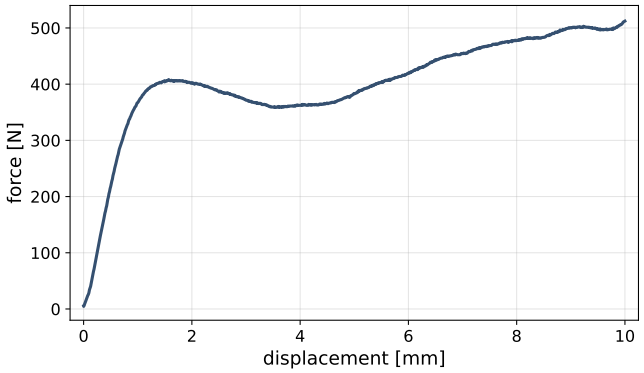


Figure 3. Experimental force–displacement response of the tetrachiral lattice specimen.

The applied force and the crosshead displacement were continuously recorded throughout the experiments. In total, three cyclic compression tests were performed. The measured force–displacement data were processed using an in-house developed MATLAB evaluation script to obtain true-stress–true-strain curves, from which the elastic modulus of $E = 860\,\mathrm{MPa}$ and yield stress of $\sigma_y = 20\,\mathrm{MPa}$ were determined.

The resulting true-stress–true-strain curves are presented in Figure 2. The experimental results exhibit excellent repeatability, with only minor differences observed between the individual specimens.

2.3. Lattice compression test

The lattice specimen was subjected to quasi-static uniaxial compression using a compact tabletop loading device with a maximum loading capacity of 2.5 kN, specifically developed for in-situ 4D X-ray computed tomography experiments on foam and lattice structures and described in detail in [27]. The experiment was performed under displacement control at a constant loading rate of $10\,\mu\mathrm{m/s}$ up to a final crosshead displacement of 10 mm.

The displacement limit used in the experiment was selected as it is the onset of the densification region in the compressive response of the studied lattice, and the experimental programme was designed to simultaneously reach the maximum achievable stroke of the loading device in this configuration. Moreover, the mechanical experiment was part of a larger experimental campaign, where in-situ 4D XCT imaging was used in the DVC evaluation pipeline to study effects such as the aging of the printed specimens on microstructural and mechanical response. Here, the selected deformation range covers the most important part of the deformation response governing the energy mitigation capabilities of the lattice.

Prior to compression, two reference XCT scans of the undeformed lattice specimen were acquired to capture the as-manufactured geometry and inspect manufacturing-induced geometric deviations. During the compression experiment, twelve additional XCT scans were performed at successive loading stages to capture the evolution of the lattice deformation.

The force–displacement response of the lattice specimen was recorded throughout the experiment and is presented in Figure 3, whereas the corresponding XCT scans of the specimen in the undeformed and final compressed configurations are shown in Figure 4. The XCT scan of the compressed specimen reveals that the deformation is not purely uniaxial. Instead, the specimen exhibits a non-uniform deformation characterized by a global buckling and lateral deflections.

3. FINITE ELEMENT MODELING

The finite element simulation of the compression of the tetrachiral lattice with nominal geometry was developed within the finite element software Abaqus [28]. The finite element model was developed step by step by defining the mesh, boundary conditions, contact interactions, material model, and solver settings.

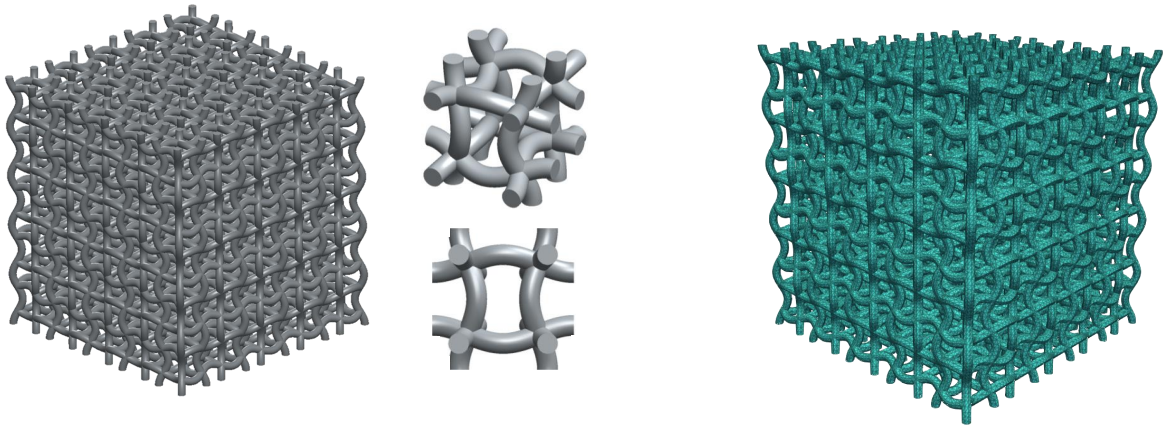
3.1. Geometry and finite element mesh

Mesh generation was performed using the ANSA preprocessing software (BETA CAE Systems) from the STL representation of the nominal CAD geometry shown in Figure 5a. A target element size of 0.3 mm was adopted throughout the lattice, following our previous studies with both implicit and explicit FEA showing that an element size of approximately half of the strut thickness yields reliable results [22], [29], [30]. Such an element sizing resulted in a finite element mesh with 1 565 967 nodes and 900 804 finite elements, as depicted in Figure 5b. The generated mesh was subsequently imported into Abaqus, where 10-node modified quadratic tetrahedral solid elements (C3D10M) were assigned for the numerical simulations. These elements are well suited for modeling complex geometries that undergo large deformations while providing improved contact performance.

The compression plates were not explicitly modeled in the numerical analysis. Instead, their effect was represented by applying



Figure 4. XCT scans of the lattice specimen in the (a) undeformed configuration, (b) final deformed configuration (isometric view), and (c) final deformed configuration (yz view).



(a) (b)

Figure 5. Finite element model of the tetrachiral lattice specimen: (a) CAD geometry and (b) finite element mesh.

appropriate boundary conditions directly to the top and bottom surfaces of the lattice. Since the compression tests were performed under quasi-static loading and the loading plates are significantly stiffer than the lattice specimen, their deformation is negligible compared with that of the specimen. Consequently, omitting the plates reduces the computational cost without significantly affecting the predicted mechanical response of the lattice.

3.2. Boundary conditions

The boundary conditions were applied directly to the lattice specimen without explicitly modeling the compression plates. All translational degrees of freedom of the nodes located on the bottom surface of the lattice were constrained. On the top surface, all translational degrees of freedom were constrained except for the vertical loading direction, in which a prescribed displacement was applied to reproduce the experimental compression test.

3.3. Contact definition

Self-contact was defined for the lattice using the general contact algorithm available in Abaqus, which accounts for interactions that develop between struts as they come into contact during large deformation. A hard contact formulation was adopted in the normal direction to prevent interpenetration of the lattice surfaces, while tangential behavior was described using the penalty friction formulation with a coefficient of friction of 0.1.

3.4. Material model

The material model was defined on the basis of the results of the cyclic compression tests performed on the bulk specimens, presented in Section 2.2.. The elastic modulus and the yield stress were determined from these experiments, resulting in values of $E = 860\,\mathrm{MPa}$ and $\sigma_y = 20\,\mathrm{MPa}$, respectively. A Poisson's ratio of 0.35 was adopted based on values commonly reported for SLA photopolymer resins [31], [32]. Plastic behavior was defined using the corresponding true-stress–plastic-strain relationship derived from the average true-stress–true-strain curve obtained from the three cyclic compression tests on the bulk specimens shown in Figure 2. The resulting true-stress–plastic-strain data are summarized in Table 2, while the selected data points are indicated on the average true-stress–true-strain curve shown in Figure 6. A material density of $1.13\,\mathrm{g/cm^3}$ was assigned according to Table 1.

3.5. Solvers

The numerical simulations were performed using the dynamic explicit solver Abaqus/Explicit to ensure robust convergence in the presence of large deformations and self-contact interactions. A smooth step amplitude was used to gradually apply the prescribed displacement and thereby minimize dynamic effects at the beginning of the analysis. To improve computational efficiency while maintaining a quasi-static response, semi-automatic mass scaling with a mass scaling factor of 10 000 was used. Throughout the analysis, the kinetic energy was monitored to verify that inertial effects remained negligible compared to the internal energy, remaining below the commonly accepted limit of 5–10 % of the internal energy, confirming that the simulations represented quasi-static loading conditions.

In addition to the explicit analysis, an implicit solution scheme (Abaqus/Standard) was also considered. Owing to its unconditional stability, the implicit solver is generally well suited for quasi-static problems and was used as a reference to verify the res-

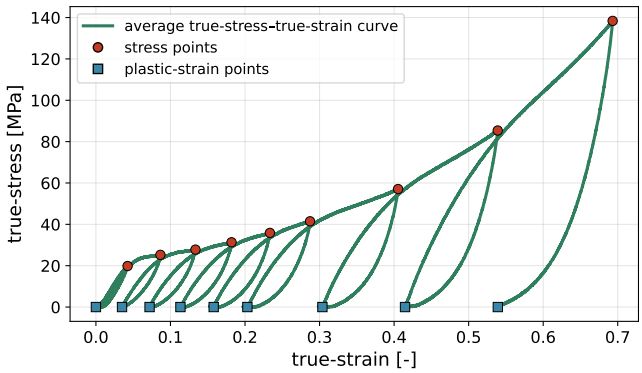


Figure 6. Average true-stress–true-strain curve and the selected stress–plastic-strain data points.

Table 2. True-stress–plastic-strain data used for the material model.

True-stress in MPa	Plastic-strain
20.00	0.00
25.24	0.04
27.78	0.07
31.32	0.11
35.85	0.16
41.47	0.20
57.06	0.30
85.36	0.41
138.38	0.54

ults obtained with the explicit formulation. The implicit solver is, however, generally more sensitive to convergence difficulties arising from complex contact interactions.

4. RESULTS AND DISCUSSION

The experimental force–displacement response of the tetrachiral lattice under uniaxial compression together with the numerical predictions obtained using the Abaqus/Explicit and Abaqus/Standard (implicit) solution schemes are presented in Figure 7.

The numerical force–displacement responses obtained using the explicit and implicit solution schemes are first compared and discussed. As shown in Figure 7, both solution schemes exhibit very good agreement throughout the initial stage of compression, with only negligible differences in the predicted response. This demonstrates that the explicit formulation accurately reproduces the quasi-static response of the lattice prior to the onset of significant contact interactions. However, once self-contact developed during compression, the implicit analysis encountered convergence difficulties and could not be continued further. Consequently, the implicit solution was limited to the initial deformation stage, whereas the explicit solver remained stable throughout the simulation.

The quasi-static nature of the explicit analysis was verified by monitoring the energy balance throughout the simulation. As shown in Figure 8, the kinetic energy remained well below 5 % of the internal energy throughout the loading process. This confirms that the applied mass scaling did not introduce significant inertial effects and that the computed response remained quasi-static.

The explicit analysis reproduces the initial compressive response of the lattice with good agreement, indicating that the adopted material model and boundary conditions provide a reasonable representation of the experimental behavior. However, as compression progresses, the numerical prediction increasingly overestimates the load-carrying capacity of the lattice. This discrepancy may be associated with the nominal geometry and idealized boundary conditions adopted in the finite element model.

The final deformed configuration at an applied displacement of 10 mm and the corresponding displacement fields predicted by the finite element model using an explicit solver are shown in Figures 9 and 10, respectively. The numerical results reveal a non-uniform deformation mode accompanied by global buckling of the lattice specimen. The displacement contours clearly illustrate the development of the deformation pattern, with lateral deflections occurring in both orthogonal planes during compression. A deformation mode that appears qualitatively comparable was also observed during the compression experiment, as shown

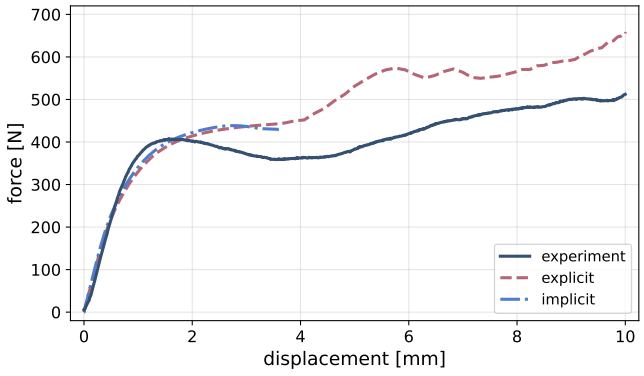


Figure 7. Comparison of the experimental and numerical force–displacement responses of the tetrachiral lattice under uniaxial compression.

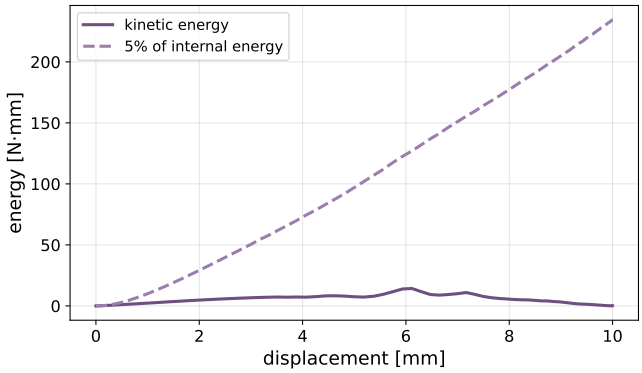


Figure 8. Comparison of the kinetic energy and 5 % of the internal energy during the explicit compression simulation.

in Figures 4b–4c. However, a quantitative validation of the predicted deformation mode requires comparison with the full-field measurements obtained from the XCT data through DVC [33], which will be addressed in future work.

4.1. Insights into manufacturing-induced geometric deviations

To examine the presence of manufacturing-induced geometric deviations, the reconstructed XCT geometry of the undeformed lattice specimen, with the loading platens removed, is superimposed on the nominal finite element geometry to facilitate comparison, as shown in Figures 11a–11b. In Figures 11a–11b, the STL-derived mesh refers to the nominal CAD geometry, whereas the XCT-adapted mesh represents the as-manufactured geometry reconstructed from the XCT data.

The nominal CAD mesh was adapted to the reconstructed XCT surface while preserving the original mesh connectivity and node numbering. Consequently, each node of the XCT-adapted mesh corresponded directly to a node of the nominal CAD mesh. Before comparison, the adapted mesh was rigidly registered to the nominal mesh using a least-squares transformation, removing only translation and rotation while preserving dimensional and local geometric differences. A small residual rigid-body misalignment, corresponding to a rotation of $0.171°$, was removed without applying any scaling. For each surface node, the deviation vector between the corresponding XCT-adapted and nominal positions was projected onto the outward normal of the nominal CAD surface. The XCT voxel size of $28.14\ \mu m$ was used to express the resulting signed normal deviations in physical units. Positive values indicate that the XCT-derived surface lies outside the nominal surface, whereas negative values indicate a local material deficit. The spatial distribution of the magnitude of these geometric deviations is shown in Figure 11c.

The mean signed normal deviation was $+42.7\ \mu m$, indicating that the XCT-derived surface was, on average, located outside the nominal surface. The mean absolute normal deviation and the corresponding RMS value were $50.5\ \mu m$ and $60.9\ \mu m$, respectively, corresponding to approximately $7.8\,\%$ and $9.4\,\%$ of the nominal strut diameter of 0.65 mm. The 5th and 95th percentiles were $-30.0\ \mu m$ and $112.9\ \mu m$, respectively, with the latter corresponding to approximately $17.4\,\%$ of the nominal strut diameter. Furthermore, $60.8\,\%$, $84.4\,\%$, and $98.7\,\%$ of the surface nodes were located within two, three, and five XCT voxels, respectively, from the nominal surface. The overall dimensions of the XCT-derived geometry exceeded the nominal dimensions by $1.44\,\%$, $1.20\,\%$, and $0.61\,\%$ in the x-, y-, and z-directions, respectively.

Although these differences appear moderate when evaluated relative to the overall specimen dimensions, the local surface deviations are non-negligible relative to the nominal strut diameter,

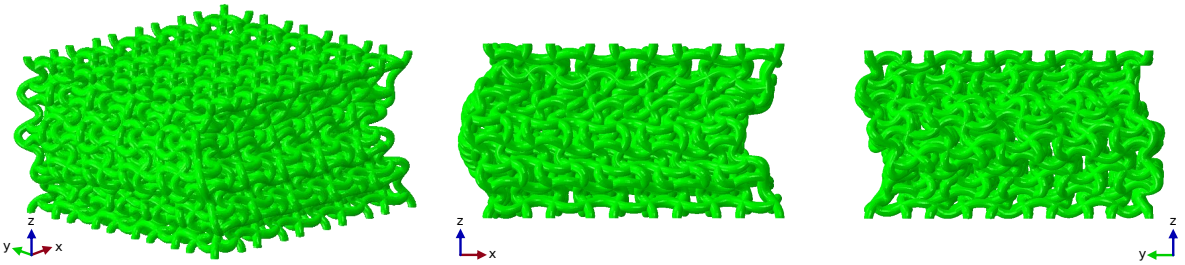


Figure 9. Final deformed configuration of tetrachiral lattice specimen predicted by the finite element model. From left to right: isometric, xz, and yz views.

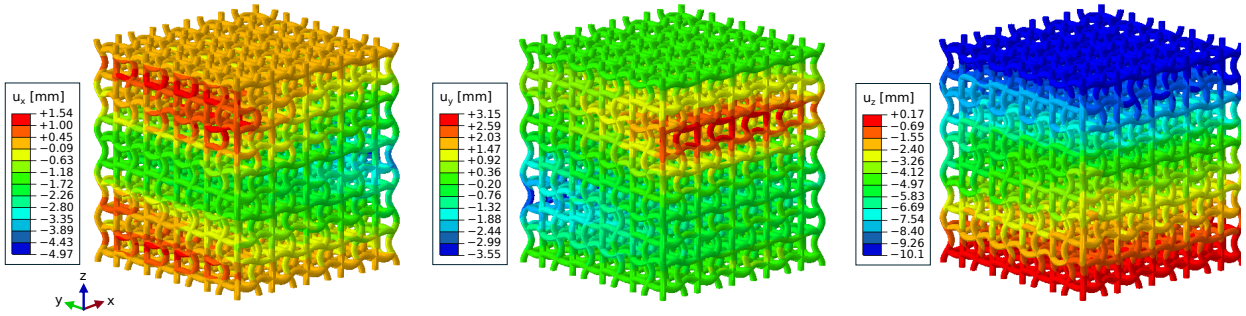


Figure 10. Final displacement fields of the tetrachiral lattice specimen predicted by the finite element model. From left to right: displacement components u_x, u_y, and u_z.

with localized variations in the strut and junction geometries. In this context, local geometric deviations may alter the deformation mechanisms of the lattice and may also cause the actual boundary conditions to deviate from the idealized conditions adopted in the numerical model. Both effects may thereby contribute to the observed discrepancy between the numerical and experimental responses.

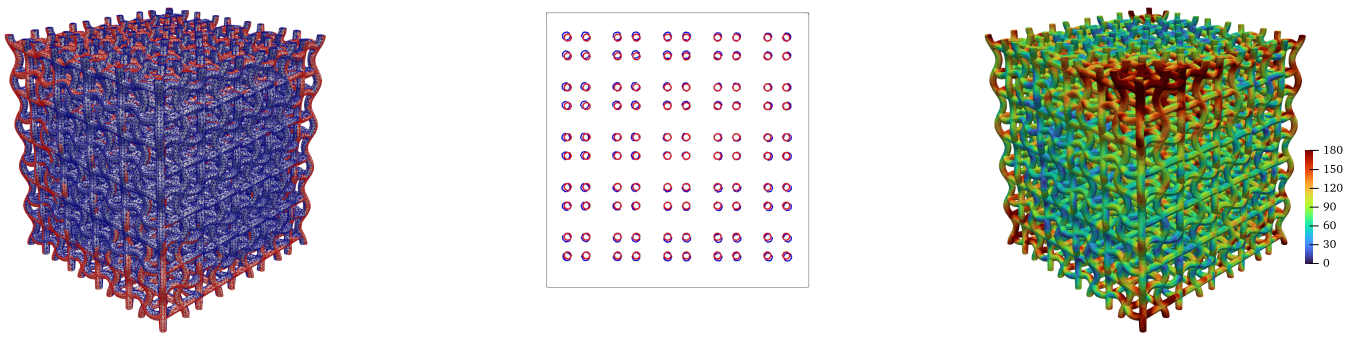
These observations highlight the importance of incorporating the as-manufactured geometry and experimentally representative boundary conditions in future numerical studies. The XCT data acquired during the compression test provide the basis for subsequent DVC analysis [24], [25]. In addition to enabling full-field measurements of the internal deformation of the lattice, DVC offers the possibility of defining experimentally derived boundary conditions, thereby enabling DVC-driven finite element analysis.

5. CONCLUSIONS

A finite element model of a nominal tetrachiral lattice subjected to a quasi-static uniaxial compression was developed and compared against experimental measurements. The model accurately reproduced the initial compressive response of the lattice, demonstrating that the adopted material model and the modeling approach provide a reasonable representation of its mechanical behavior. However, the predicted load-carrying capacity became increasingly overestimated with increasing compression, indicating the limitations of the idealized numerical model.

Quantitative comparison of the reconstructed XCT geometry with the nominal CAD geometry showed that the manufacturing-induced geometric deviations were non-negligible at the strut scale, with localized variations in the strut and junction geometries. These geometric deviations may contribute to the increasing discrepancy between the numerical and experimental responses.

The present study establishes a baseline numerical model for the compressive response of tetrachiral lattices with nominal geometry. Future work will focus on incorporating the reconstructed XCT geometry together with experimentally representative boundary conditions derived from the DVC analysis of XCT data, enabling image-based finite element analyzes for a more accurate prediction of the mechanical response of additively manufactured lattice structures.



(a) (b) (c)

Figure 11. Comparison of the nominal STL-derived finite element mesh and the XCT-adapted mesh after rigid registration: (a) isometric overlay of the nominal mesh (red) and the XCT-adapted mesh (blue); (b) mid-height cross-section in the xy-plane; (c) magnitude of the nodal geometric deviation between corresponding surface nodes, expressed in μm.

AUTHORS' CONTRIBUTION

V. Topić Brečević: Formal analysis, Writing – review & editing; **E. Hadzalic:** Conceptualization, Formal analysis, Writing – original draft; **V. Drechslerová:** Design and manufacture of specimens; Writing – review & editing; **P. Koudelka:** Conceptualization; Writing – review & editing; Funding acquisition **D. Kytýř:** Investigation; Writing – review & editing; **Z. Tomičević:** Conceptualization; Investigation; Writing – review & editing

DATA AVAILABILITY STATEMENT

Representative experimental data supporting this study are publicly available in the Zenodo repository DOI: 10.5281/zenodo.21669226.

ACKNOWLEDGMENT

This research was supported by the Czech Science Foundation (Project No. 25-18209S), the Strategy AV21 programme "AI: Artificial Intelligence for Science and Society", and the European Union (NextGenerationEU) under the National Recovery and Resilience Plan 2021–2026 (NRRP), through the UNIZAG FSB institutional project "Generative design based on experimental and numerical modelling - GENEXPERT", approved by the Ministry of Science, Education and Youth of the Republic of Croatia (component C3.2, source 581).

REFERENCES

[1] A. Alderson, K. L. Alderson, D. Attard, K. E. Evans, R. Gatt, J. N. Grima, W. Miller, N. Ravirala, C. W. Smith, K. Zied, Elastic constants of 3-, 4- and 6-connected chiral and anti-chiral honeycombs subject to uniaxial in-plane loading, Composites Science and Technology, vol. 70, 2010, no. 7, pp. 1042–1048.
DOI: 10.1016/j.compscitech.2009.07.009

[2] J. Wu, Y. Zhang, F. Yang, F. Jiang, X. Xu, Y. Tan, L. Su, A hybrid architectural metamaterial combining plate lattice and hollow-truss lattice with advanced mechanical performances, Additive Manufacturing, vol. 76, 2023, p. 103764.
DOI: 10.1016/j.addma.2023.103764

[3] M. Zhang, C. Zhao, G. Li, K. Luo, Mechanical properties of the composite lattice structure with variable density and multi-configuration, Composite Structures, vol. 304, 2023, p. 116405.
DOI: 10.1016/j.compstruct.2022.116405

[4] W. Zhang, H. Yin, Y. Wu, Q. Jin, L. Wu, G. Wen, J. Liu, X. Wu, A novel auxetic 3D lattice structure for enhancing energy absorption, Composite Structures, vol. 326, 2023, p. 117620.
DOI: 10.1016/j.compstruct.2023.117620

[5] L. Yue, H. Liu, Z. Cheng, Q. Kan, G. Kang, Dynamic crushing behavior of a novel bi-directional gradient lattice structure under axial and oblique impact loadings, Thin-Walled Structures, vol. 198, 2024, p. 111697.
DOI: 10.1016/j.tws.2024.111697

[6] W. Wu, D. Qi, H. Liao, G. Qian, L. Geng, Y. Niu, J. Liang, Deformation mechanism of innovative 3D chiral metamaterials, Scientific Reports, vol. 8, 2018, no. 1, p. 12575.
DOI: 10.1038/s41598-018-30737-7

[7] F. Runkel, G. Ramstein, G. Molinari, A. F. Arrieta, P. Ermanni, Mechanics of curved-ligament hexachiral metastructures under planar deformations, Journal of the Mechanics and Physics of Solids, vol. 125, 2019, pp. 145–163.
DOI: 10.1016/j.jmps.2018.12.001

[8] A. Mauko, T. Fíla, J. Falta, P. Koudelka, V. Rada, M. Neuhäuserová, P. Zlámal, M. Vesenjak, O. Jiroušek, Z. Ren, Dynamic deformation behaviour of chiral auxetic lattices at low and high strain-rates, Metals, vol. 11, 2021, no. 1, p. 52.
DOI: 10.3390/met11010052

[9] M. Chen, R. Zhong, Y. Wang, H. Wu, M. Fu, Mechanical properties of re-entrant chiral anisotropic honeycomb, Engineering Structures, vol. 291, 2023, p. 116431.
DOI: 10.1016/j.engstruct.2023.116431

[10] Y. Xue, W. Wang, F. Han, Enhanced compressive mechanical properties of aluminum based auxetic lattice structures filled with polymers, Composites Part B: Engineering, vol. 171, 2019, pp. 183–191.
DOI: 10.1016/j.compositesb.2019.05.002

[11] H. Zhou, K. Jia, X. Wang, M.-X. Xiong, Y. Wang, Experimental and numerical investigation of low velocity impact response of foam concrete filled auxetic honeycombs, Thin-Walled Structures, vol. 154, 2020, p. 106898.
DOI: 10.1016/j.tws.2020.106898

[12] Q. Gao, W.-H. Liao, Energy absorption of thin walled tube filled with gradient auxetic structures: Theory and simulation, International Journal of Mechanical Sciences, vol. 201, 2021, p. 106475.
DOI: 10.1016/j.ijmecsci.2021.106475

[13] J. X. Qiao, C. Q. Chen, Impact resistance of uniform and functionally graded auxetic double arrowhead honeycombs, International Journal of Impact Engineering, vol. 83, 2015, pp. 47–58.
DOI: 10.1016/j.ijimpeng.2015.04.005

[14] N. Novak, K. Hokamoto, M. Vesenjak, Z. Ren, Mechanical behaviour of auxetic cellular structures built from inverted tetrapods at high strain rates, International Journal of Impact Engineering, vol. 122, 2018, pp. 83–90.
DOI: 10.1016/j.ijimpeng.2018.08.001

[15] C. Boursier Niutta, R. Ciardiello, A. Tridello, Experimental and numerical investigation of a lattice structure for energy absorption: Application to the design of an automotive crash absorber, Polymers, vol. 14, 2022, no. 6, p. 1116.
DOI: 10.3390/polym14061116

[16] M. Smith, Z. Guan, W. J. Cantwell, Finite element modelling of the compressive response of lattice structures manufactured using the selective laser melting technique, International Journal of Mechanical Sciences, vol. 67, 2013, pp. 28–41.
DOI: 10.1016/j.ijmecsci.2012.12.004

[17] G. Campoli, M. S. Borleffs, S. Amin Yavari, R. Wauthle, H. Weinans, A. A. Zadpoor, Mechanical properties of open-cell metallic biomaterials manufactured using additive manufacturing, Materials & Design, vol. 49, 2013, pp. 957–965.
DOI: 10.1016/j.matdes.2013.01.071

[18] M. Karamooz Ravari, M. Kadkhodaei, M. Badrossamay, R. Rezaei, Numerical investigation on mechanical properties of cellular lattice structures fabricated by fused deposition modeling, International Journal of Mechanical Sciences, vol. 88, 2014, p. 154–161.
DOI: 10.1016/j.ijmecsci.2014.08.009

[19] C. S. Ha, M.-T. Hsieh, The effect of geometric imperfections on the mechanical response of isotropic closed-cell plate lattices, Mechanics Research Communications, vol. 128, 2023, p. 104073.
DOI: 10.1016/j.mechrescom.2023.104073

[20] X. Cao, Y. Jiang, T. Zhao, P. Wang, Y. Wang, Z. Chen, Y. Li, D. Xiao, D. Fang, Compression experiment and numerical evaluation on mechanical responses of the lattice structures with stochastic geometric defects originated from additive-manufacturing, Composites Part B: Engineering, vol. 194, 2020, p. 108030.
DOI: 10.1016/j.compositesb.2020.108030

[21] M. Park, M. P. Venter, A. D. Plessis, Simulation of the compression testing of additively manufactured lattice structures using inputs from microcomputed tomography, Material Design & Processing Communications, vol. 2023, 2023, p. 8000727.
DOI: 10.1155/2023/8000727

[22] P. Koudelka, P. Zlámal, T. Fíla, K. Souček, V. Rada, M. Neuhäuserová, J. Šleichrt, D. Kytýř, Analysis of a 3D tetrachiral auxetic lattice under compression: Combining experimental and numerical approaches of 4D X-ray microtomography, digital volume correlation, and finite element modeling, Emergent Materials, vol. 8, 2025, pp. 2345–2364.
DOI: 10.1007/s42247-024-00973-x

[23] O. Jiroušek, P. Zlámal, D. Kytýř, M. Kroupa, Strain analysis of trabecular bone using time-resolved X-ray microtomography, Nuclear Instruments and Methods in Physics Research Section A: Accelerators, Spectrometers, Detectors and Associated Equipment, vol. 633, 2011, p. S148–S151.
DOI: 10.1016/j.nima.2010.06.151

[24] Z. Tomičević, F. Hild, S. Roux, Mechanics-aided digital image correlation, The Journal of Strain Analysis for Engineering Design, vol. 48, 2013, no. 5, pp. 330–343.
DOI: 10.1177/0309324713482457

[25] A. Vrgoč, Z. Tomičević, B. Smaniotto, F. Hild, Characterization of glass fiber reinforced polymer via digital volume correlation: Quantification of strain activity and damage growth, Composites Science and Technology, vol. 234, 2023, p. 109932.
DOI: 10.1016/j.compscitech.2023.109932

[26] Phrozen Technology Co., Ltd., Phrozen RPG Resin User Guide, Phrozen Technology Co., Ltd., 2024. Online. [Accessed: 2026-06-29].
https://3d.nice-cdn.com/upload/file/User_Guide_RPG_Resin_EN.pdf

[27] T. Fíla, J. Šleichrt, D. Kytýř, I. Kumpová, M. Vopálenský, P. Zlámal, V. Rada, D. Vavřík, P. Koudelka, S. Senck, Deformation analysis of the spongious sample in simulated physiological conditions based on in-situ compression, 4D computed tomography and fast readout detector, Journal of Instrumentation, vol. 13, Nov. 2018, no. 11, p. C11021–C11021.
DOI: 10.1088/1748-0221/13/11/c11021

[28] Abaqus Analysis User's Guide, Dassault Systèmes Simulia Corp., Providence, RI, USA, 2024.

[29] J. Šleichrt, J. Falta, M. Neuhäuserová, V. Drechslerová, P. Koudelka, V. Rada, T. Fíla, O. Jiroušek, Instrumented dynamic penetration of sandwich panels with auxetic and non-auxetic core using direct impact hopkinson bar, Advanced Engineering Materials, vol. 25, 2023, no. 24.
DOI: 10.1002/adem.202300980

[30] P. Koudelka, P. Zlámal, T. Doktor, V. Drechslerová, R. Dvořák, T. Fíla, Experiments and numerical modeling of dynamic compressive response in auxetic lattices 3D printed from 316L stainless steel, Emergent Materials, vol. 9, 2026, no. 10, p. 239.
DOI: 10.1007/s42247-026-01531-3

[31] Y. Gao, X. Wei, X. Han, Z. Zhou, J. Xiong, Novel 3D auxetic lattice structures developed based on the rotating rigid mechanism, International Journal of Solids and Structures, vol. 233, 2021, p. 111232.
DOI: 10.1016/j.ijsolstr.2021.111232

[32] Y. Li, Z. Teng, Effect of printing orientation on mechanical properties of SLA 3D-printed photopolymer, Fatigue & Fracture of Engineering Materials & Structures, vol. 47, 2024, no. 5, pp. 1531–1545.
DOI: 10.1111/ffe.14265

[33] A. Mandić, V. Kosin, C. Jailin, Z. Tomičević, B. Smaniotto, F. Hild, Damage detection in a polymer matrix composite from 4D displacement field measurements, Materials, vol. 16, 2023, no. 18, p. 6300.
DOI: 10.3390/ma16186300